Supporting information

Glutathione-triggered release of SO2 gas to augment oxidative stress for enhanced chemodynamic and sonodynamic therapy

Ya Tian[†a], Pei Li[†b], Likai Wang [a], Xueli Ye [a], Zhonghuan Qu [a], Juan Mou [a], Shiping Yang [a], Huixia Wu* [a]*

[a] The Education Ministry Key Lab of Resource Chemistry, Joint International Research Laboratory of Resource Chemistry, Ministry of Education, Shanghai Key Laboratory of Rare Earth Functional Materials, Shanghai Municipal Education Committee Key Laboratory of Molecular Imaging Probes and Sensors, and Shanghai Frontiers Science Center of Biomimetic Catalysis, College of Chemistry and Materials Science, Shanghai Normal University, Shanghai 200234, China

[b] Department of Ultrasound, Shanghai Institute of Medical Imaging, Zhongshan Hospital, Fudan University, Shanghai 200032, China

[†] Authors who contribute equally

*Co-corresponding authors: Juan Mou, Email: moujuan@shnu.edu.cn; Huixia Wu, Email: wuhuixia@shnu.edu.cn.

Experiment Section

Materials and Reagents

All chemical reagents were used without any further purification. Iron(III) acetylacetonate ($Fe(acac)_3$) and triethylamine (TEA) were provided by Adamas Reagents, Ltd. 2,4-dinitrobenzenesulfonyl chloride (DNsCl) was purchased from

Sigma-Aldrich. 3-Aminopropyltriethoxysilane (APTES) was received from Thermo Fisher Scientific. Dichloromethane (CH_2Cl_2), ethanol (C_2H_5OH, 99%), and urea (CH_4N_2O) were purchased from Greagent (Shanghai, China). Ammonium hydroxide (NH_4OH) and tetraethyl orthosilicate (TEOS) were bought from Sinopharm Chemical Reagent Co., Ltd. (Shanghai, China). GSH and GSSG assay kit (S0053), GPX assay kit (S0056), and MDA assay kit (S0131S) were purchased from Beyotime (Shanghai, China). Deionized water obtained by a Millipore purification device (18.2 MΩ cm) was used in all experiments.

Characterization

Transmission electron microscopy (TEM) images were obtained using JEOL JEM-2199 transmission electron microscope operated at 200 kV with an energy-dispersive spectrometer (EDS). Scanning electron microscopic (SEM) images were recorded on a field-emission scanning electron microscope (FE-SEM, S-4800, Hitachi). UV-vis absorption spectra were performed on a DU 730 BeckMan UV-vis-NIR spectrometer. Fourier-transform infrared (FTIR) spectra were received from a spectrophotometer (Nicolet Avatar 370 FTIR). Fluorescence spectra were acquired on a Cary Eclipse fluorescence spectrofluorimeter. N_2 adsorption-desorption isotherms were recorded on a Micromeritics Tristar 3000 instrument at 77 K. The surface area and pore diameter distribution were determined by Brunauer–Emmett–Teller (BET) and Barrett–Joyner–Halenda (BJH) methods. Hydrodynamic diameter and Zeta potentials were determined using a Malvern Zetasizer Nano ZS (Malvern EEN 3690). The flow cytometry analysis was carried out on a BeckMan cyan XDP flow cytometer. The confocal laser scanning microscopic images were recorded on a confocal microscope (Leica TCs SP5). The *in vitro* and *in vivo* MR imaging experiments were performed in 0.5 T (NMI20-Analyst) and 1.0 T (NM42-040H-I) MRI systems, respectively.

Supplementary Figures

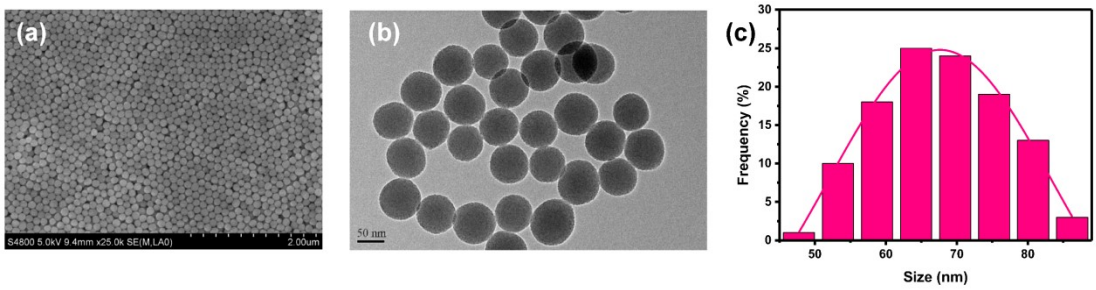

Fig. S1. SEM (a), TEM (b) images, and size distribution (c) of SiO_2 NPs.

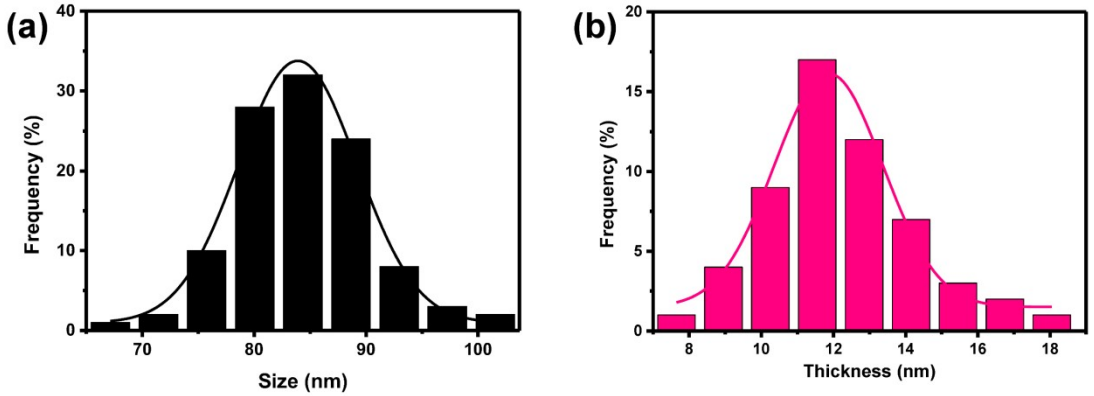

Fig. S2. The size (a) and shell thickness (b) distributions of FH NPs.

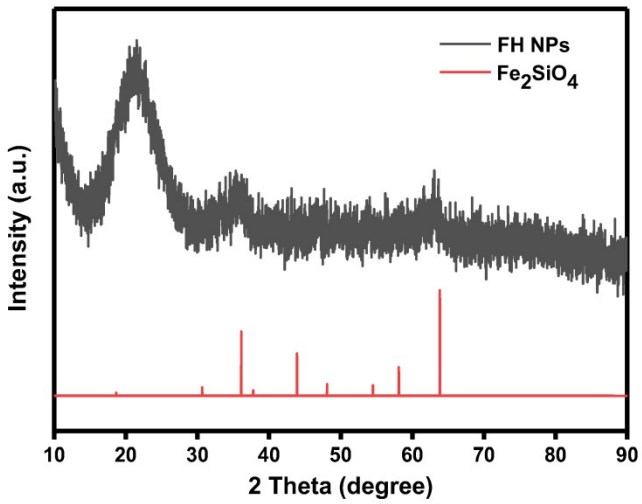

Fig. S3. XRD patterns of FH NPs.

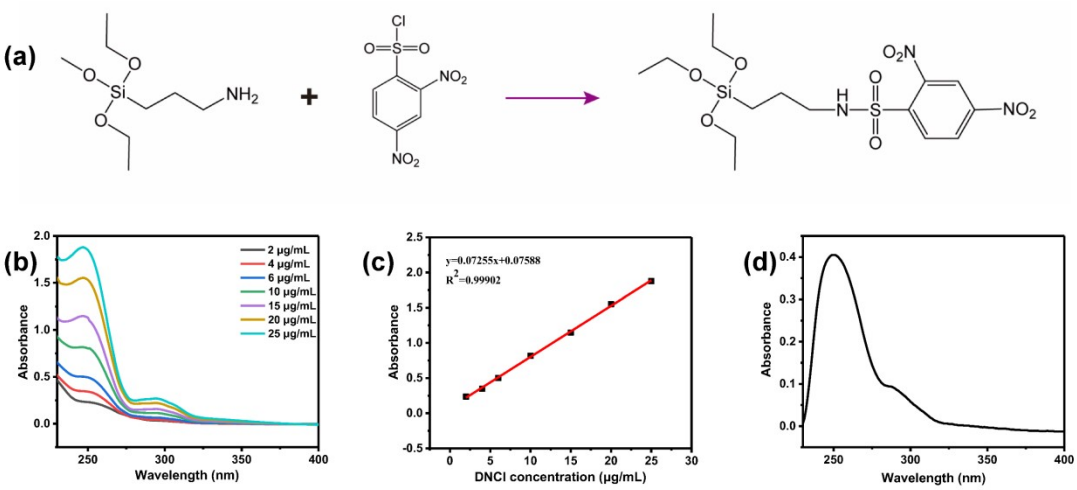

Fig. S4. (a) The attachment of SO_2 prodrug. (b) UV–Vis absorption spectra of DNs with different concentrations. (c) The standard curve of DNs. (d) UV–Vis absorption spectra of residual DNs in the supernatant solution.

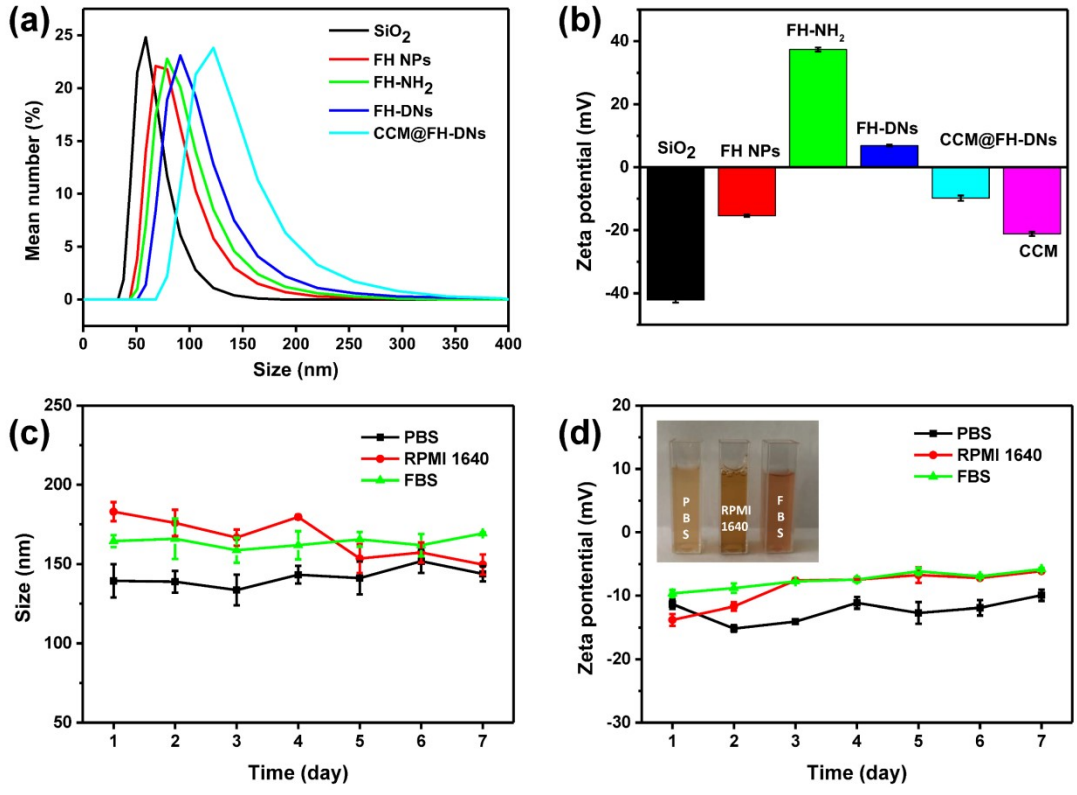

Fig. S5. DLS distribution (a) and Zeta potential (b) of the as-synthesized nanoparticles. Time-monitored DLS distributions (c) and Zeta potentials (d) of CCM@FH-DNs for 7 days. Inset: Photograph of CCM@FH-DNs dispersed in different medium solutions during 7 days' storage.

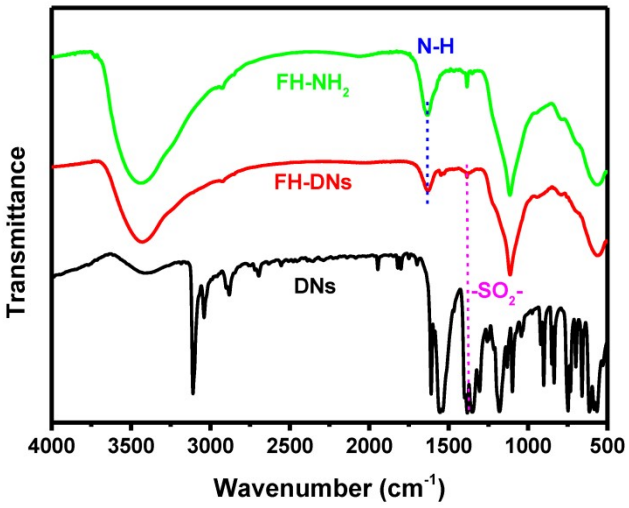

Fig. S6. FTIR spectra of FH-NH_2, FH-DNs, and DNs.

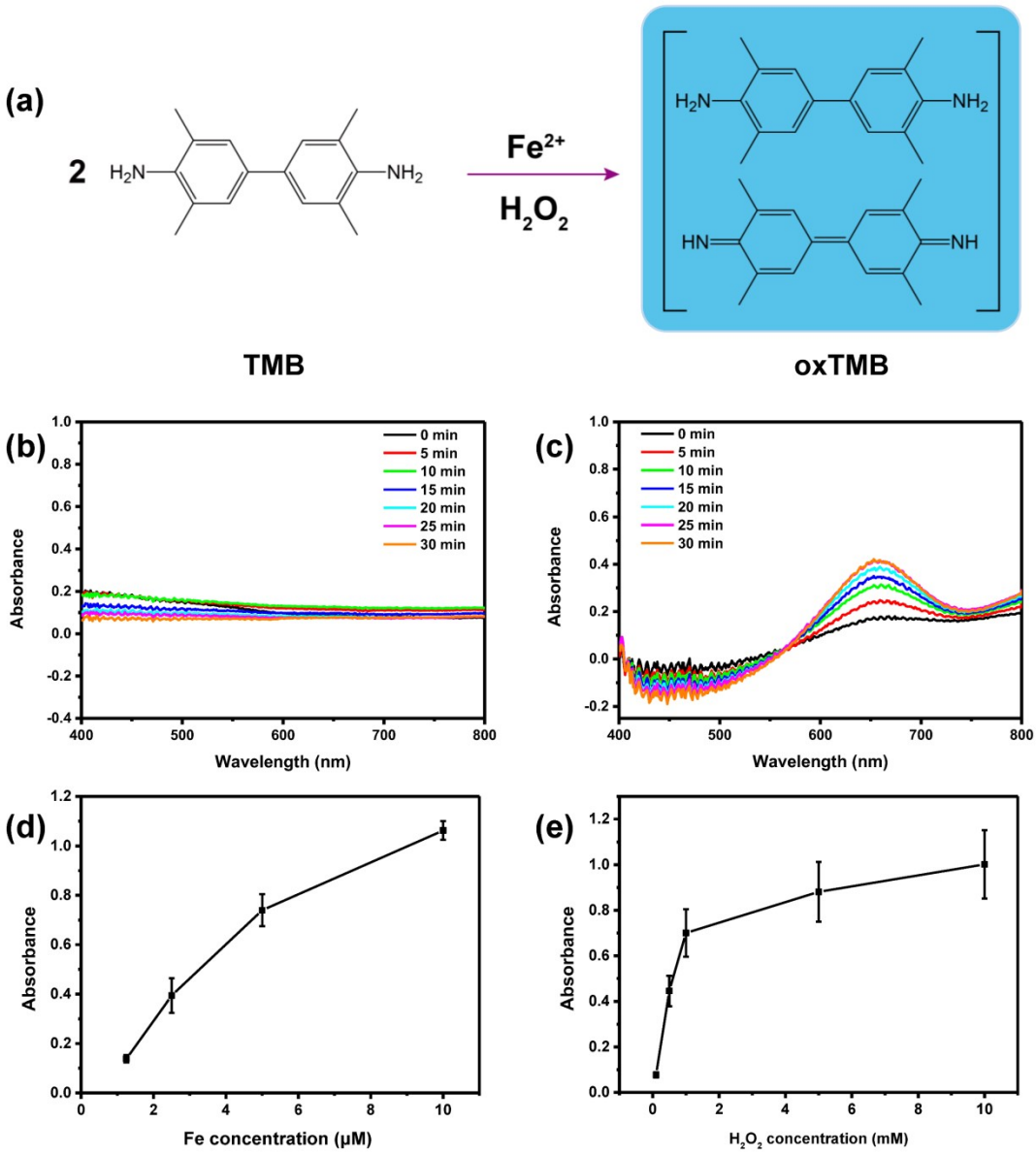

Fig. S7. (a) The reaction scheme of TMB oxidation by •OH. The Fenton reaction of FH NPs at pH=7.4 buffer solution (b) and pH=6.3 buffer solution (c) detected by TMB. (d) Fenton reaction of FH NPs with different concentrations of FH NPs at fixed H_2O_2 concentration (pH=5.2 buffer solution). (e) Fenton reaction of FH NPs at different concentrations of H_2O_2 (pH=5.2 buffer solution).

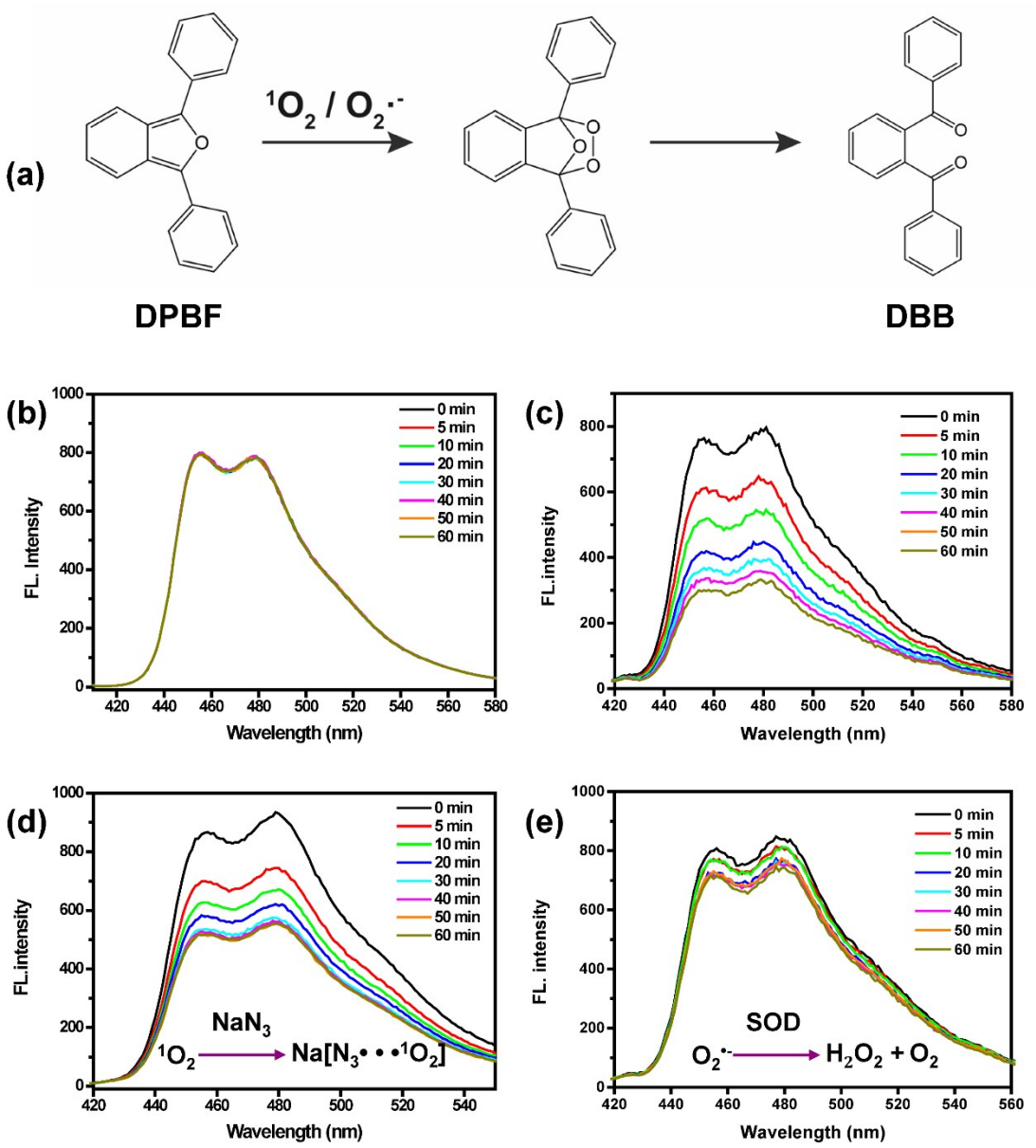

Fig. S8. (a) Schematic illustration of the oxidation of DPBF by $^1O_2$ and $O_2^{\bullet-}$. Fluorescence spectra of DPBF (b), and in the presence of FH NPs (c), FH NPs+NaN_3 (d), and FH NPs + SOD (e) upon US irradiation for different intervals.

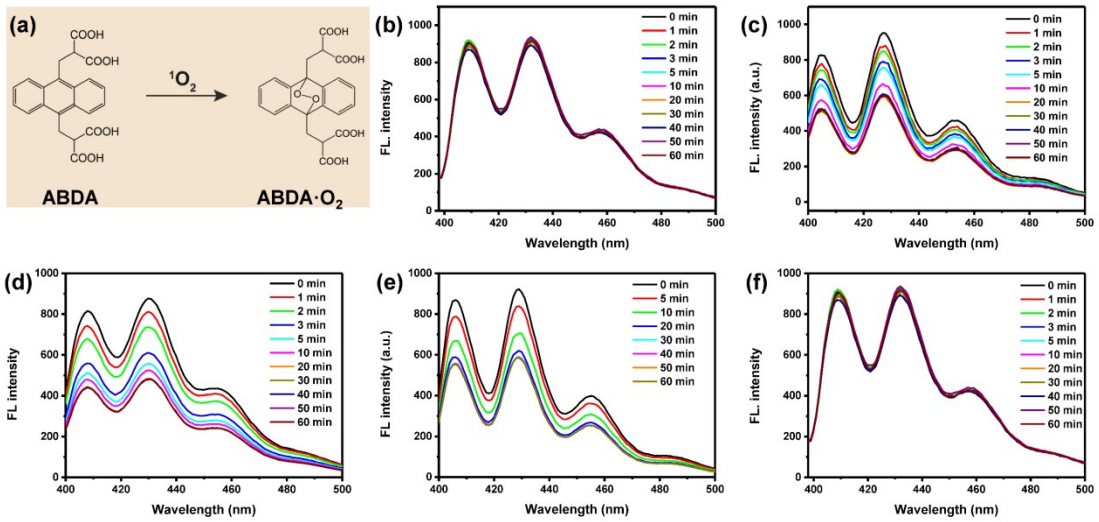

Fig. S9. The reaction of ABDA with $^1O_2$. Fluorescence intensity spectra of ABDA (b), and in the presence of FH NPs (c), FH-DNs (d), CCM@FH-DNs (e), and CCM@FH-DNs+NaN_3 (f) upon US irradiation for different intervals.

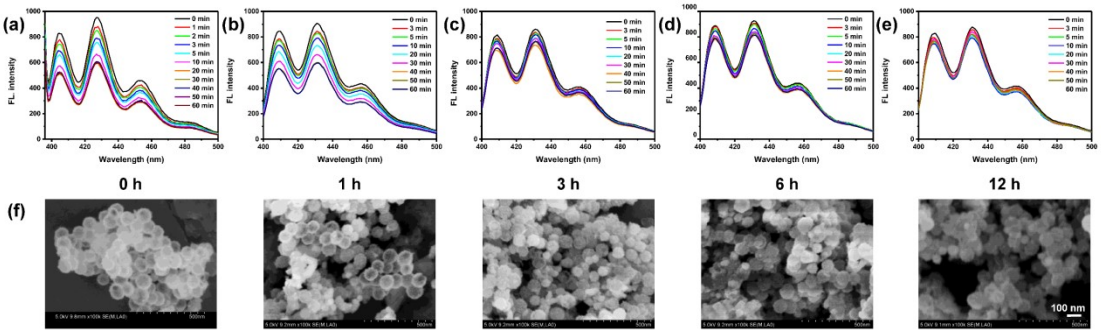

Fig. S10. Effect of cavity structure collapse of FH NPs on SDT (indicator: ABDA). Fluorescence intensity spectra of FH NPs incubated in pH=6.3 buffer solution for 0 h (a), 1 h (b), 3 h (c), 6 h (d), and 12 h (e), respectively. (f) SEM comparison of FH NPs after different incubation periods. Scale bar: 100 nm.

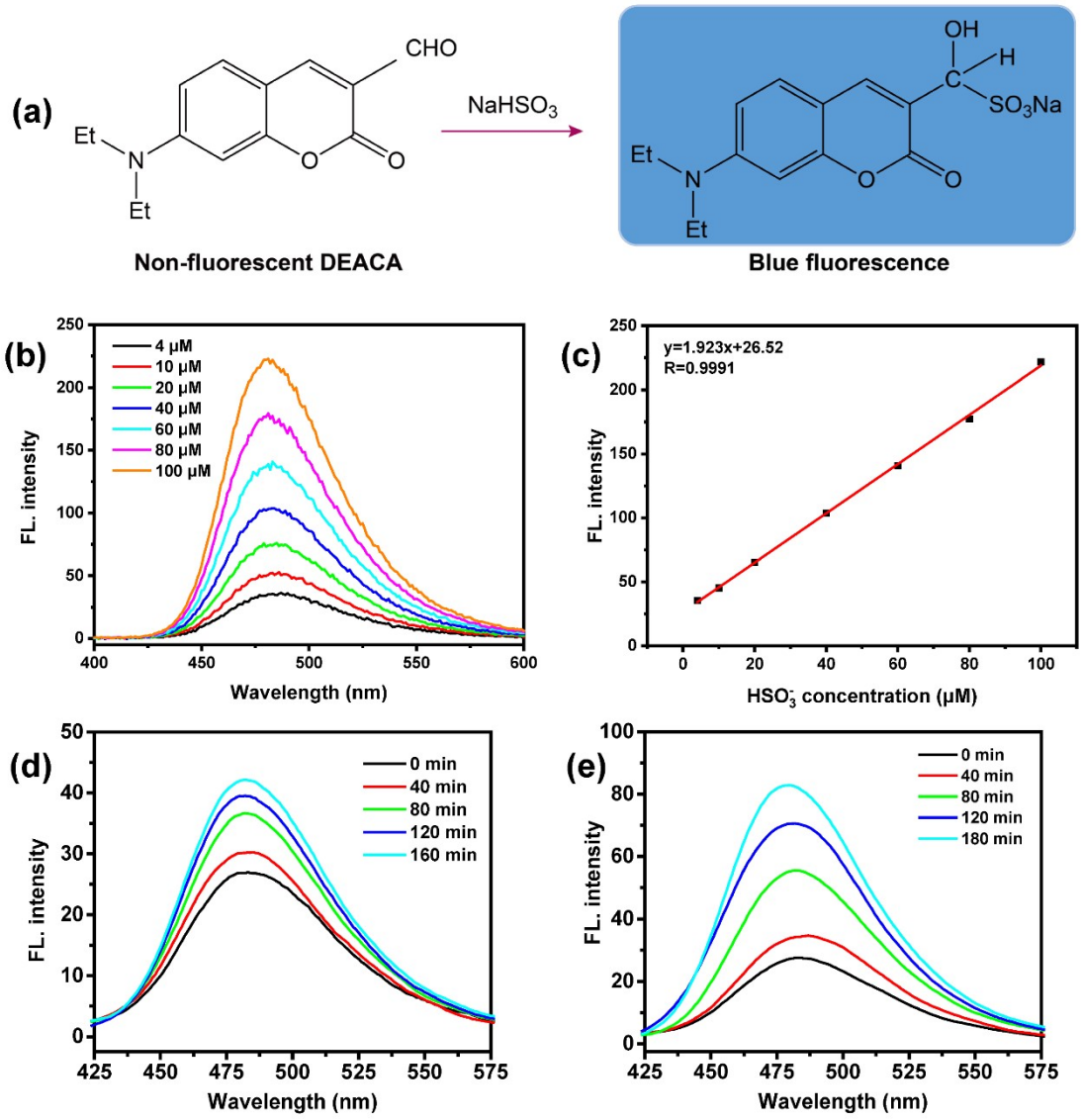

Fig. S11. (a) The detection principle of the DEACA indicator. (b) Fluorescence intensity spectra of DEACA reacted with different concentrations of $NaHSO_3$ solution. (c) The standard curve for the detection of HSO_3^-. Fluorescence intensity spectra of DEACA and CCM@FH-DNs in the presence of (d) 5 mM and (e) 10 mM Cys with time-released HSO_3^-.

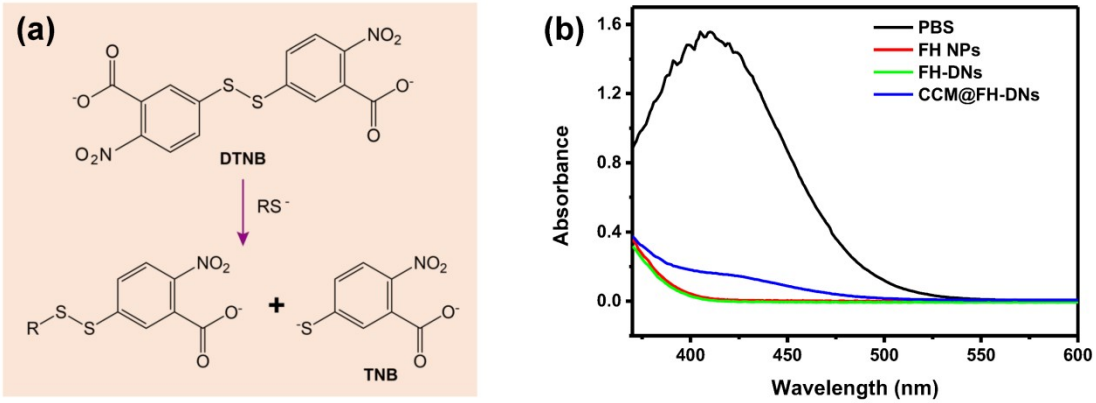

Fig. S12. (a) Schematic illustration of reaction between DTNB and a thiol. (b) UV-Vis absorption spectra of PBS buffer solution, FH NPs, FH-DNs, and CCM@FH-DNs incubated with GSH for 12 h.

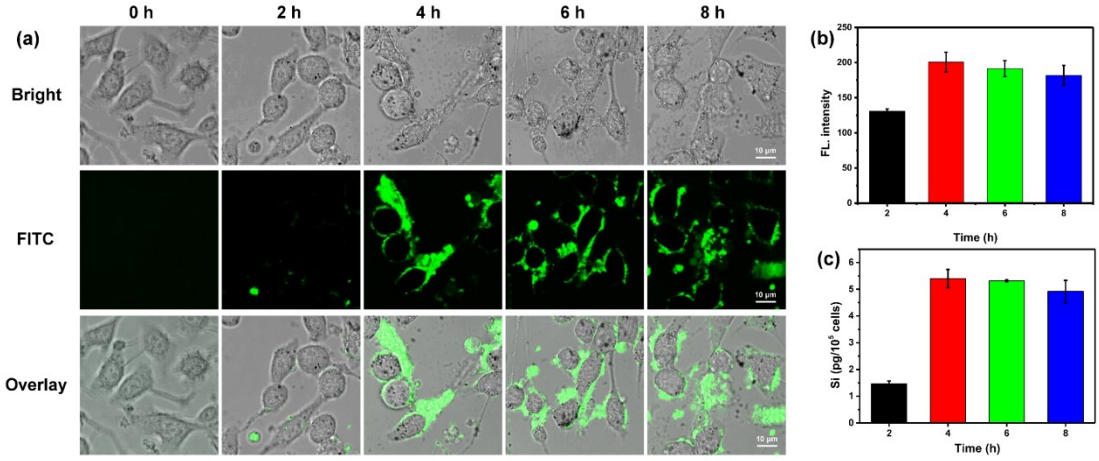

Fig. S13. (a) CLSM images of 4T1 cells after treatment with prestained CCM@FH-FITC (20 μg/mL) for different periods. Scale bar: 10 μm. Quantitative analysis of intracellular uptake by 4T1 cells using fluorescence (b) and ICP-AES (c) measurement, respectively.

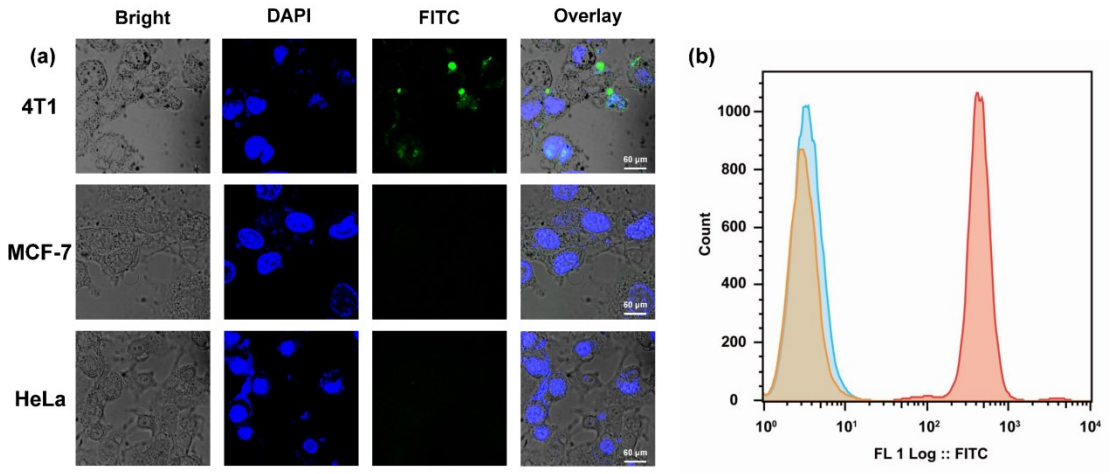

Fig. S14. CLSM images (a) and flow cytometry (b) of 4T1, MCF-7, and HeLa cells incubated with CCM@FH-DNs for 4 h.

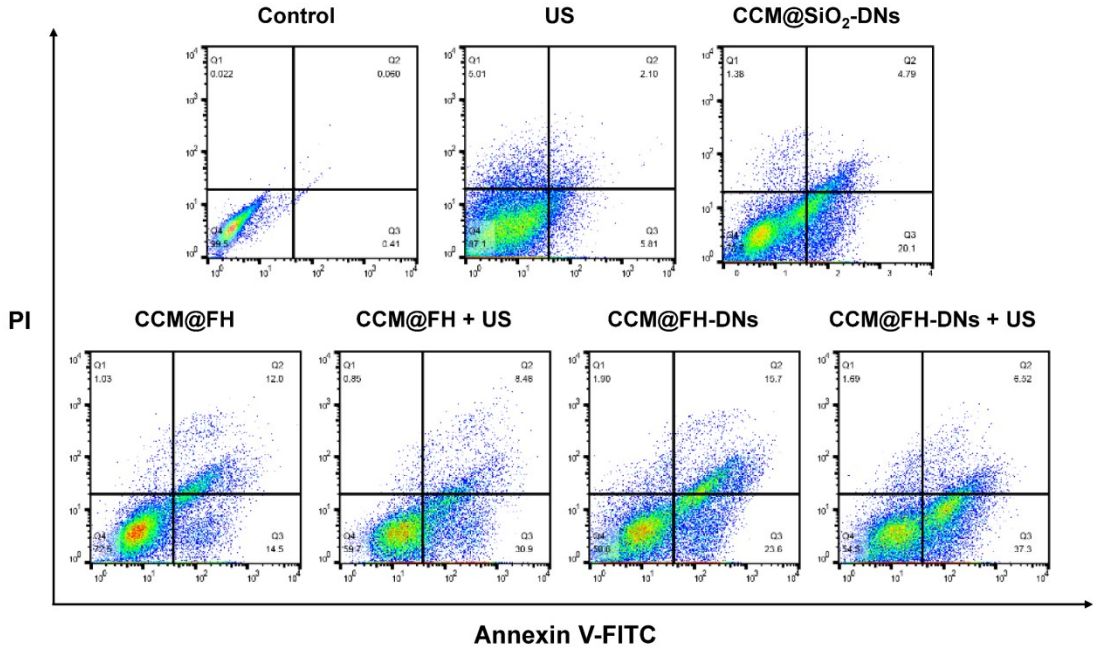

Fig. S15. Flow cytometry data to evaluate apoptosis levels in 4T1 cells after different treatments.

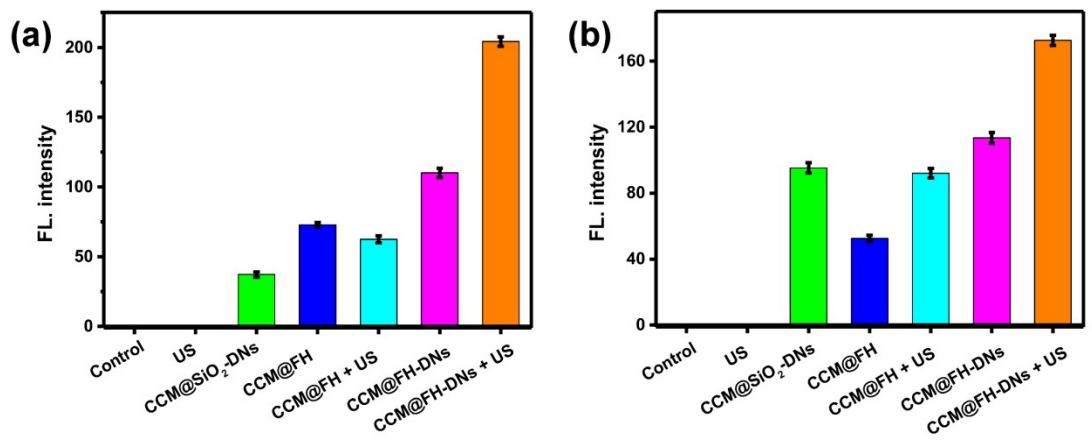

Fig. S16. Quantitative analysis of intracellular ROS (a) and $O_2^{\bullet-}$ (b) levels in different groups.

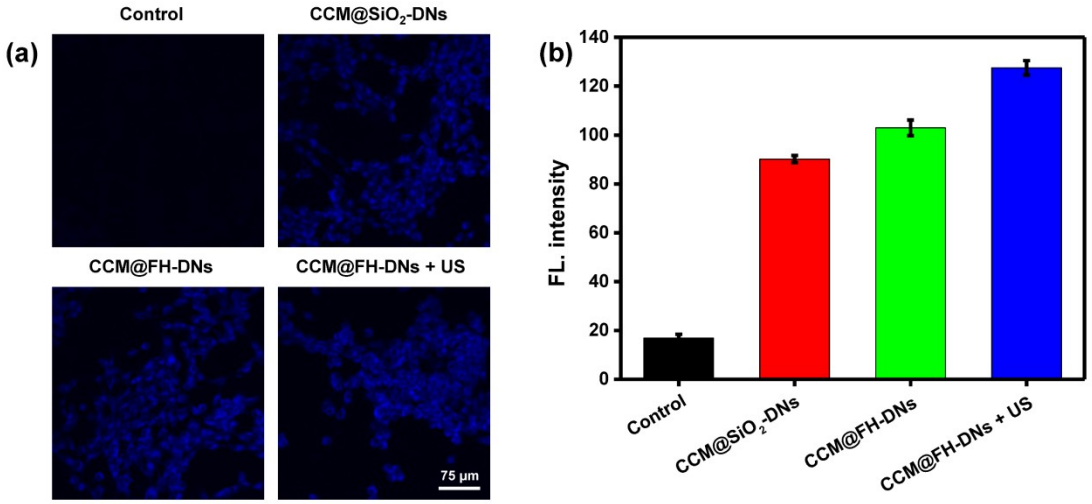

Fig. S17. SO_2 production detection in 4T1 cells after different treatments by CLSM (a) and corresponding quantitative analysis (b). [Fe]: 5 μM, [SO_2]: 40 μM. Scale bar: 75 μm.

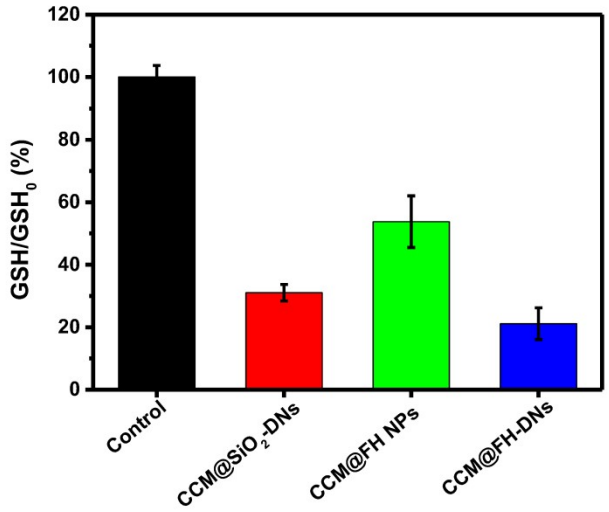

Fig. S18. Intracellular GSH level detection of 4T1 cells after different treatments.

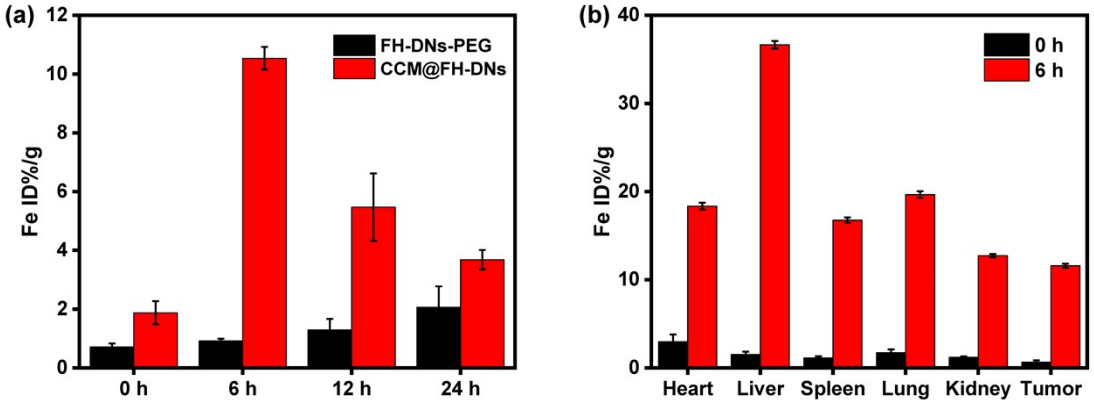

Fig. S19. (a) Fe content of tumor sites after tail vein injection of CCM@FH-DNs and FH-DNs-PEG for different periods. (b) *In vivo* biodistribution of Fe in tumors and major organ tissues of the tumor-bearing mice before and 6 h post-injection of CCM@FH-DNs.

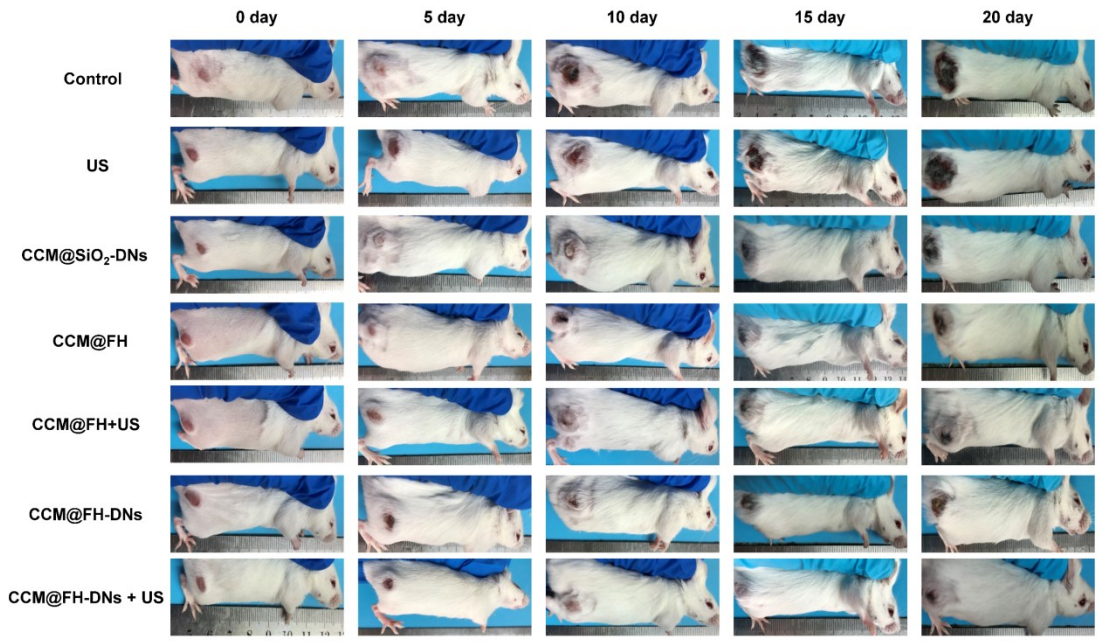

Fig. S20. Photographs of mice during treatment.

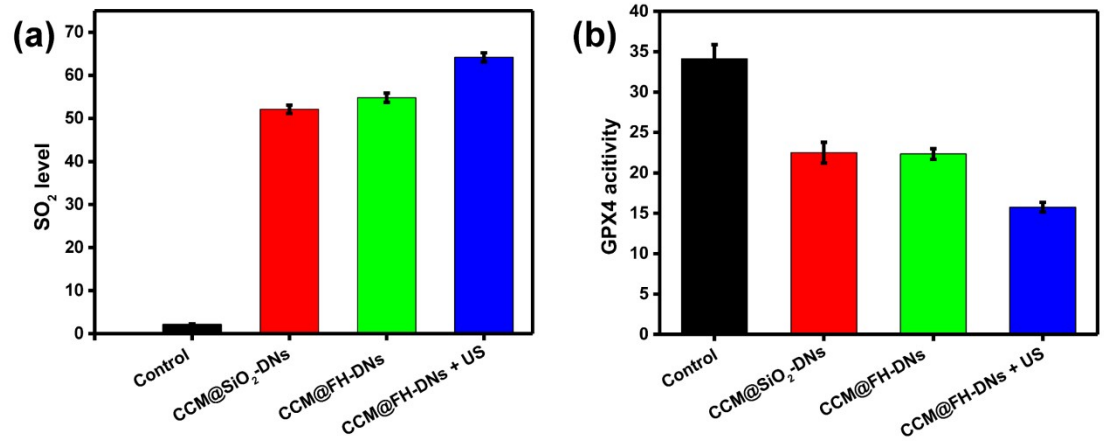

Fig. S21. Quantitative analysis of SO_2 production (a) and GPX4 activity (b) in tumor of mice after different treatments.

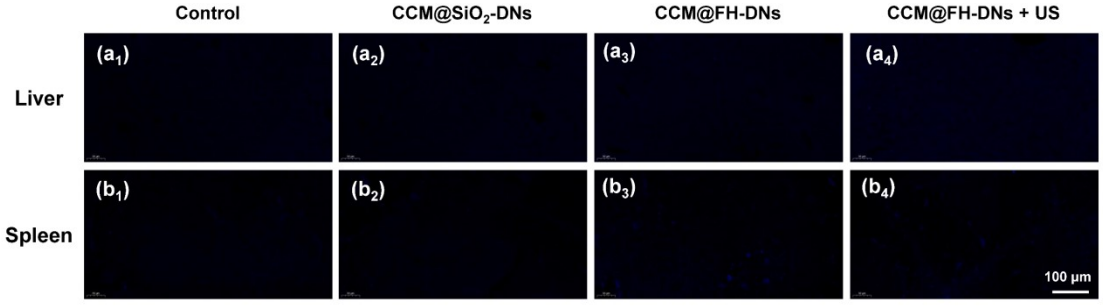

Fig. S22. SO_2 production in the liver (a) and spleen (b) of mice after different treatments. Scale bar: 100 μm.

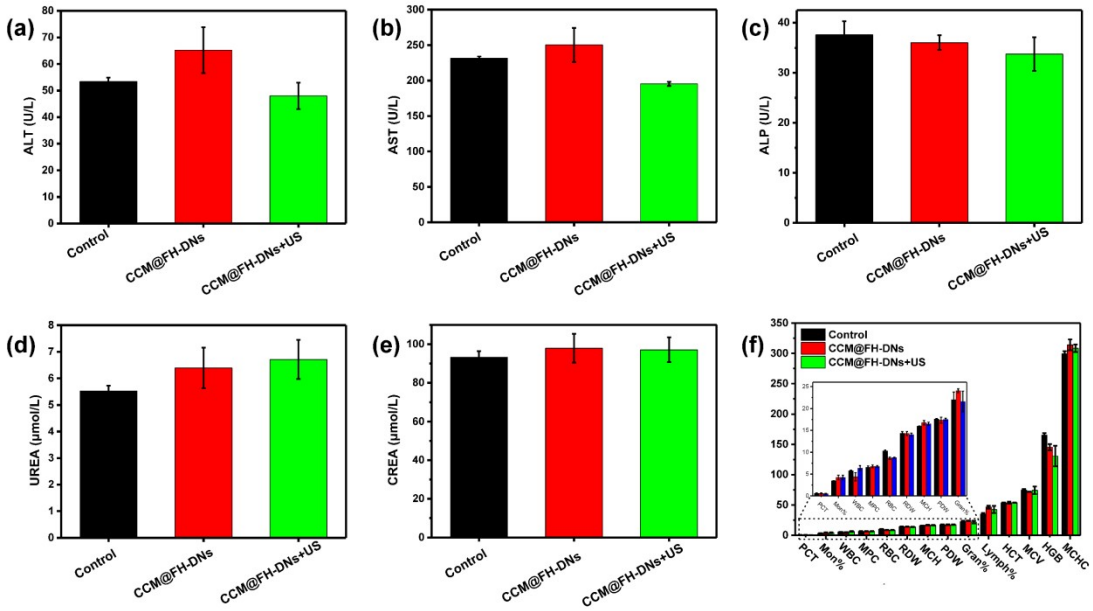

Fig. S23. Blood levels of ALT (a), AST (b), and ALP (c) as markers of liver function. Blood UREA (d) and CREA (e) as markers of kidney function. (f) Key indicators of the routine blood test of the mice after different treatments.

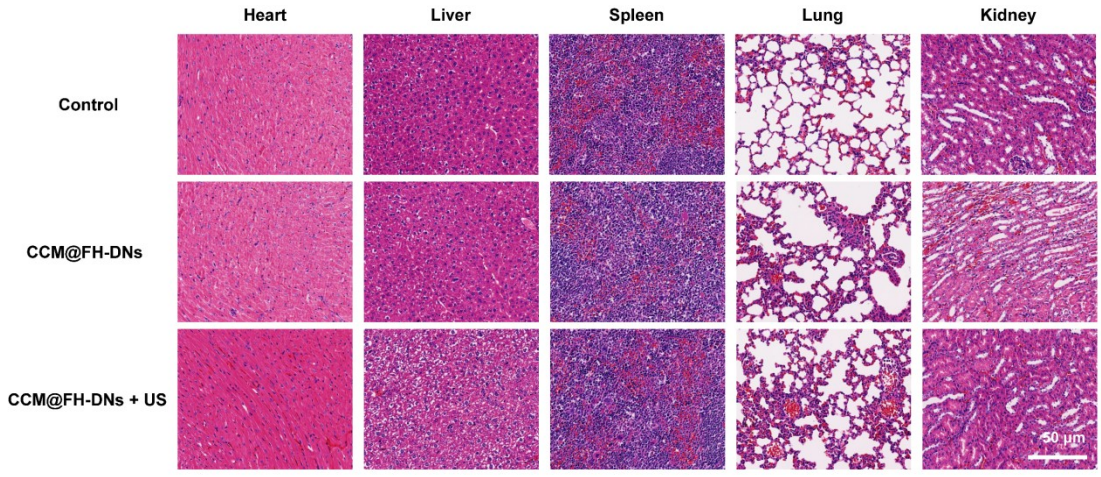

Fig. S24. H&E-stained tissue sections from the major organs (heart, liver, spleen, lung, and kidney) of mice after different treatments. Scale bar: 50 μm.